Structural characterization of mechanically milled ZnO: influence of zirconia milling media

Structural characterization of mechanically milled ZnO: influence of zirconia milling media

K Vojisavljević[1], M Šćepanović[2], T Srećković[1], M Grujić-Brojčin[2], Z Branković[1] and G Branković[1]

[1] Institute of Multidisciplinary Research, Kneza Višeslava 1, 11030 Belgrade, Serbia
[2] Center for Solid State Physics and New Materials, Institute of Physics, Pregrevica 118, 11080 Belgrade, Serbia

E-mail: katarina@cms.bg.ac.yu (K Vojisavljević)

Abstract

Zinc oxide nanoparticles were obtained by milling in a planetary ball mill with a zirconia milling assembly for up to 5 h in air. The samples were characterized by scanning electron microscopy, x-ray diffraction (XRD) and Raman spectroscopy methods. The deviation of the lattice parameters from single crystal values was related to defect creation and increase of strain inside the hexagonal lattice of milled ZnO nanoparticles. The observed redshift and peak broadening of the major first-order Raman modes were ascribed to the formation of intrinsic defects by mechanical milling combined with the effects of phonon confinement in nanosized powders. To investigate the type of intrinsic defects and impurities introduced during milling, it was necessary to analyze both milled and thermally treated ZnO. After thermal treatment, the intensity of the Raman spectra increased and the peak positions reverted to values similar to those in unmilled ZnO powder, pointing to defect annihilation. XRD patterns of sintered samples confirmed the existence of zirconia impurities and the Rietveld analysis revealed a small amount of zirconium introduced in the ZnO crystal lattice on the Zn sites or interstitial sites. The large influence of those impurities on the micro-Raman spectra of thermally treated samples was observed in this study.

1. Introduction

Zinc oxide (ZnO) is a versatile, multifunctional material and one of the most promising materials in the family of wide-gap semiconductors [1]. Due to its unique properties, such as optical transparency, high piezoelectric properties, chemical, radiation and thermal resistance, it has been extensively used in lot of industrial products (ceramics, rubber additives, pigments) and medical applications [2–5]. Recently, the discovery of the piezoelectric, and photocatalysis properties of ZnO nanostructures has triggered several new applications [6–8]. Various physical and chemical routes have been used to prepare a wide range of ZnO nanostructures, including novel ZnO nanoarchitectures [9]. ZnO has an extremely large exciton binding energy of 60 meV, which allows an efficient excitonic lasing mechanism to operate at room temperature. Therefore, zinc oxide in the form of pressed powders and polycrystalline films deposited on various substrates attracts a great deal of attention [10].

Milling in high-energy mills is one of the methods for preparation of nanocrystalline powders and, in particular, ZnO powder [11–15]. Different terms are commonly used in the literature to denote the processing of powder particles in high-energy mills, but most frequent are mechanical activation, mechanical milling and mechanical alloying [16]. Mechanical milling is the method most often used in powder obtaining technology, as it is a very efficient and relatively inexpensive method in contrast to chemical (wet and dry) technologies. If the milling assembly is carefully selected, including the milling media and parameters, it is possible to obtain large amounts of powder, with accurate control of particle and crystallite size, amount and types of defects and impurities [16, 17].

Prolonged milling in high-energy mills is necessary for obtaining nanoparticles, but it leads to contamination of

the starting material. Since the milling process tends to contaminate powder, it can be used as an additional route for introducing the milling assembly material as the desired dopant into a powder. Our previous investigations showed that Fe ions are incorporated in zinc oxide milled in a vibro-mill with steel rings. The influence of these defects both on microstructural and electrical properties of ZnO was observed [12, 13]. In this paper the structural characteristics of ZnO nanopowders obtained by mechanical milling in a planetary ball mill with zirconium oxide vials and balls were investigated. Known as a transition metal oxide, ZrO_2 is commonly used in producing milling tools. Therefore we intended to introduce it into ZnO during the ball milling process and investigate the influence of *in situ* addition of ZrO_2 on the structural and electrical changes in mechanically milled ZnO. Namely, it was found that the ZrO_2–ZnO binary oxide can be used as the catalysts [18]. Also, ZnO/ZrO_2 powders are useful materials for the preparation of ceramic targets for thin film deposition by the radio frequency magnetron sputtering method and pulsed-laser deposition [19, 20]. The Zr-doped ZnO films prepared by this method can be used as transparent conducting oxide films with a variety of applications in microelectronic systems.

In the present research, the results of both x-ray powder diffraction analysis and Raman spectroscopy were analyzed. The aim of the investigation was to examine the influence of zirconia milling media on the structural changes in ZnO during mechanical milling. To complete the information about intrinsic defects and impurities and their influence on properties of ZnO nanoparticles, it was necessary to analyze both milled and thermally treated ZnO powders. For that purpose, Raman and micro-Raman spectroscopy, as well as the resistivity measurements, were performed. The results shown in this work will be beneficial for a better understanding of similar types of systems in the future.

2. Experimental conditions

The starting material was commercial zinc oxide (ZnO, Kemika) powder with 99.96% purity, specific surface area (S_{sp}) of 3.6 $m^2\,g^{-1}$ and particle size between 200 and 400 nm. This powder was milled in zirconia vials with zirconia balls of 10 mm diameter, using a planetary ball mill (Fritsch Pulverisette 5). It is well known that the proper choice of milling parameters, such as milling time, ball-to-powder mass ratio and rotation speed have a major role in the preparation of very small ZnO nanoparticles. For example, starting with as-received ZnO powders with particle size of $\sim$100 nm some authors have proposed a long milling time (30–32 h) with ball-to-powder mass ratio 10:1, or short milling time (3 h) with ball-to-powder mass ratio 35:1 for production of $\sim$25 to 15 nm sized ZnO nanoparticles [21–23]. Our recent investigation showed that the microstructural characteristics of mechanically milled ZnO powder strongly depend on milling conditions, i.e. ball-to-powder mass ratio and time of milling (t) [24]. For that reason, the milling process in this study was performed in a continual regime in air, following these conditions: the rotation speed of the disk was 400 rpm, ball-to-powder mass ratio was

40:1, t was 30, 90 or 300 min. Milled powders are marked as ZnO-p-t. Before the sintering process, all powders were compacted by the uniaxial double pressing technique under a pressure of 589 MPa to form cylindrical samples (pellets) with a green density in the range of 60–70% ρ_T. Those samples were sintered in an air atmosphere in a tubular furnace (Lenton LT 818), with a constant heating rate of 15 °C/min, from room temperature to 1100 °C followed by a holding time of 2 h. Sintered samples were marked as ZnO-s-t.

The morphology of the powders was studied using a scanning electron microscope (SEM, Jeol JSM-5800). For these measurements, the powders were ultrasonically dispersed in alcohol and the obtained suspensions were deposited on the sample holder. The morphology of polished and thermally etched sintered samples was observed by SEM (VEGA TS 5130 MM).

The x-ray diffraction patterns were collected on a diffractometer (Norelco-Philips PW-1050) using Cu Kα (1.540 60 nm) radiation. The divergence slit of 1°, receiving slit of 0.1 mm and Soller slit system of 5.1° were used for all measurements. The collections were done in step scan mode (step size $2\theta = 0.02°$, counting time 5 s per step) in angular range $2\theta = 28°$–80°. Structural refinement analyses of x-ray diffraction data collected from zinc oxide powders and sintered samples were performed using the Topas-Academic software [25].

Raman measurements of powders (slightly compacted to pellets) and sintered pellets were performed at room temperature in the backscattering geometry using the 442 nm line of a He–Cd laser, Jobin-Yvon U1000 double monochromator and a photomultiplier as a detector. The photoluminescence spectrum of sintered sample (ZnO-s-300) was measured with the same equipment and laser line. Micro-Raman spectra of all sintered samples were recorded by a Jobin-Yvon T64000 triple spectrometer system, equipped with a confocal microscope and a nitrogen-cooled CCD detector. The 514 nm laser line of an Ar^+ laser was used as the excitation source.

Resistivities of all sintered samples were determined after fitting of impedance spectra measured by an impedance analyzer (Gamry EIS300).

3. Results and discussion

3.1. Microstructural and structural properties

The XRD patterns of ZnO-p-0 and ZnO-p-300 powders are shown in figure 1. All peaks in figure 1 match the ZnO wurtzite structure (JCPDS card 36-1451, space group $P6_3mc$) for both presented powders. There are no additional peaks in the XRD pattern of milled ZnO powder. The substantial broadening and decrease of diffraction peak intensities obtained for ZnO-p-300 can be attributed to the mechanical milling, which leads to the reduction of average particle/crystallite size and an increase of strain inside the crystallite. Further, in this XRD pattern all diffraction peak positions are shifted to higher angles, indicating a slight change in lattice parameters. The increase of intrinsic defect concentration and the possible existence of
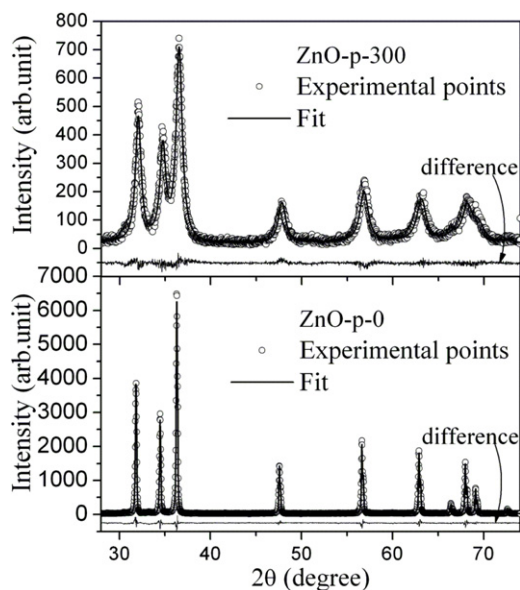
Figure 1. The XRD patterns of powders ZnO-p-0 and ZnO-p-300.

Table 1. Structural refinement results of unmilled and milled powders and sintered ZnO.

	Lattice parameters		Crystallite size (nm)	Strain (%)
	a (Å)	c (Å)		
ZnO-p-0	3.2502(1)	5.2071(2)	190	0
ZnO-p-300	3.2601(2)	5.2170(2)	15	1.54
ZnO-s-0	3.2530(1)	5.2077(1)	500	0.05
ZnO-s-30	3.2540(1)	5.2088(2)	377	0.04
ZnO-s-90	3.2540(1)	5.2094(3)	354	0.10
ZnO-s-300	3.2554(1)	5.2114(1)	204	0.18

lattice (3.2498 Å and 5.2066 Å, for a- and c-axes respectively). After 300 min of milling (ZnO-p-300), the deviation of lattice parameters (3.2601, 5.2170 Å) from single crystal values points to the creation of defects and an increase of strain in ZnO powder. Also, such an increase of lattice parameters indicates possible substitution of Zn by Zr ions, (Zr_{Zn}) [20].

XRD spectra of sintered samples are shown in figure 3(a). It was found that the distinct additional peaks, although very small, belong to the monoclinic (M, JCPDS card no. 89-9066, space group $P2_1/c$) and tetragonal (T, JCPDS card no. 79-1769, space group $P4_2/nmc$) phase of ZrO_2. Obviously, ZrO_2 existed in the milled powders before compacting and sintering, since it was detected in the sintered samples of ZnO-s-t ($t = 30$, 90 and 300 min) in the form of inclusions.

To analyze the gradual increase of ZrO_2 content with increase of milling time, Rietveld analysis was performed on the set of sintered samples (figure 3(a)). The most important results shown in figure 3(b) and summarized in table 1 indicate a slight increase of ZrO_2 content in the form of inclusions with increase of milling time. Beside the deviation of ZnO lattice parameters of sintered samples ZnO-s-t ($t = 30$, 90 and 300 min) from the parameters of sintered ZnO-s-0, slight peak shifting in the XRD spectra of m-ZrO_2 from typical values ($2\theta = 28.213°$, 40.766°, 44.798°, 45.573°, 50.616°) to the lower positions ($2\theta = 28.174°$, 40.671°, 44.580°, 45.426°, 50.552°), which correspond to $ZnZrO_3$ (JCPDS no. 32-1482) is also registered. Both effects point to a small number of Zr^{4+} ions introduced into the ZnO crystal lattice on Zn^{2+} sites, or Zn interstitial sites. After all, it is very important to note that

some impurities introduced into the powder during mechanical milling could be responsible for the above-mentioned behavior. To examine the presence of the defects and impurities in ZnO nanoparticles, as well as the strain formed during the milling, the Rietveld analyses were performed on XRD spectra of both powders. The obtained results are presented in table 1.

First of all, the Rietveld analysis shows that the average crystallite size drastically decreases from 190 nm (ZnO-p-0) to 15 nm (ZnO-p-300) due to the intensive mechanical process. The SEM images shown in figure 2 confirm these results. Namely, a high level of shape anisotropy and particle sizes in the range from 100 to 500 nm are observed in ZnO-p-0. On the other hand, the milling process remarkably changes the morphology of powders through ball-to-ball and ball-to-vial collisions in the planetary ball mill, leading to the appearance of fine particles and a decrease in the average particle size to a value below 20 nm in ZnO-p-300.

The results presented in table 1 also show that the starting powder is unstrained and that the values of its lattice parameters are similar to those expected for an ideal ZnO
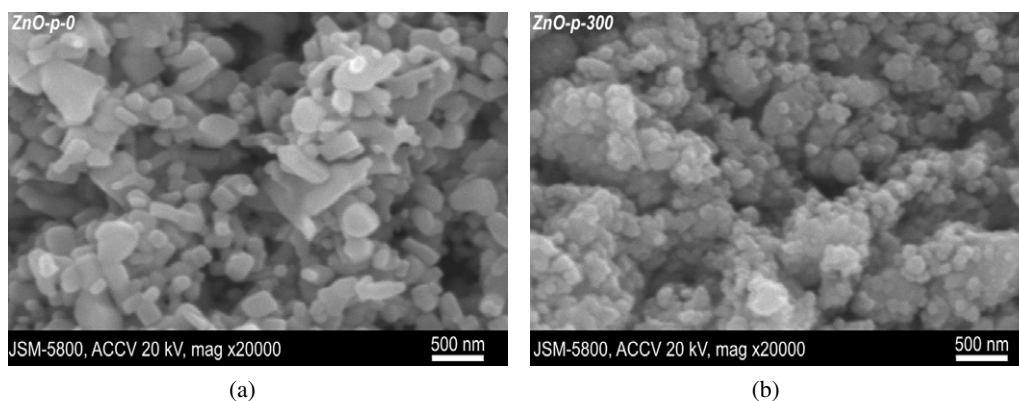

| (a) | (b) |

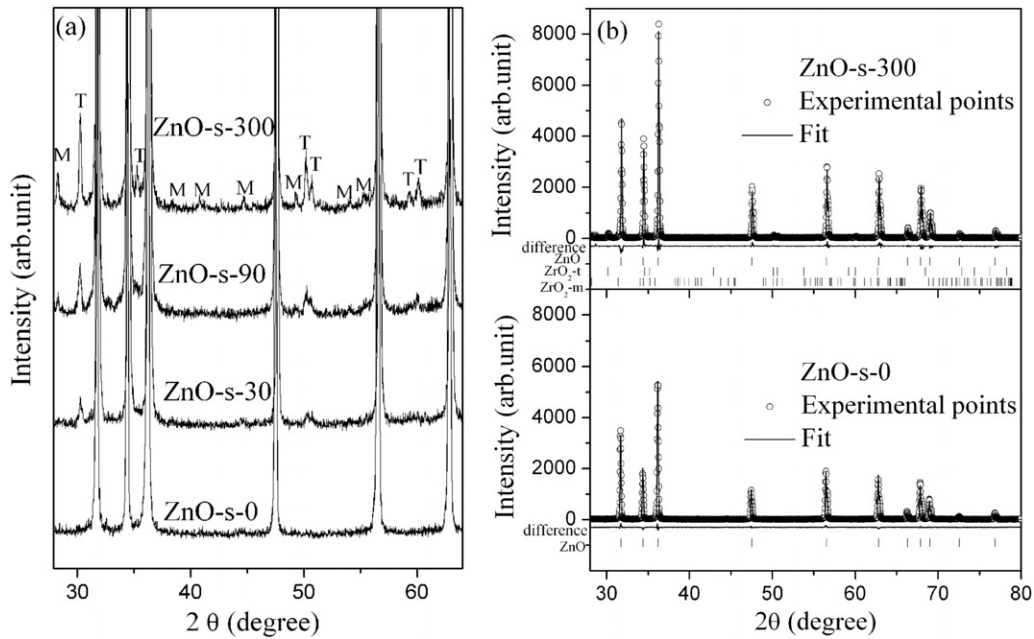**Figure 2.** SEM images of powders ZnO-p-0 and ZnO-p-300.

Figure 3. Enlarged XRD pattern of all ZnO sintered samples with assigned positions of t-ZrO$_2$ and m-ZrO$_2$ (a) and fitted spectra of ZnO-s-0 and ZnO-s-300 (b). The difference between observed and calculated values is presented by the lines below both patterns. Peak positions of different phases are shown as small tick bars at the baseline.

the change of the ZnO lattice parameters (shown in table 1) in both milled powder (ZnO-p-300) and sintered samples ZnO-s-t (t = 30, 90 and 300 min) could not be attributed to the difference between the ionic radii of Zr^{4+} (0.73 Å) and Zn^{2+} (0.74 Å). It was rather assigned to the increase of the repulsive interaction between Zr^{4+} and the second nearest Zn^{2+} [26].

The quantity of each phase of ZrO$_2$ was determined by Rietveld analysis and is presented in table 2. The slight increase of both ZrO$_2$ phases with increasing milling time is evident. The m-ZrO$_2$ phase was not observed in the ZnO-s-30 sample.

Also, it was found that the strain in sintered ZnO samples drastically decreases in comparison to its value in starting powders, as shown in table 1. This indicates that strain relaxation takes place during the sintering process. Note that the strain values in sintered ZnO samples with greater ZrO$_2$ content slightly increase, while the crystallite size decreases. Opposite to our results, a slight increase of crystallite size was detected in Zr-doped ZnO thin films with increase of ZrO$_2$ content from 0 to 5 wt% [19].

3.2. Raman spectra of powders and sintered samples

Raman spectra of unmilled and milled ZnO powders, as well as spectra of the samples obtained by sintering of compacts prepared from those powders were measured by a Jobin-Yvon U1000 Raman system using the 442 nm line of a He–Cd laser. Spectra of ZnO-p-0 and ZnO-p-300 powders and sintered samples of ZnO-s-0 and ZnO-s-300 are shown in figure 4.

It is known for wurtzite-type ZnO (space group $P6_3mc$) that optical phonons at the Γ point of the Brillouin zone belong to the following irreducible representation: $\Gamma_{\text{opt}} = A_1 + E_1 + 2E_2 + 2B_1$, where A_1 and E_1 modes are both

Table 2. Weight per cent of ZnO, t-ZrO$_2$ and m-ZrO$_2$ phase in sintered ZnO samples.

	ZnO phase (wt%)	t-ZrO$_2$ phase (wt%)	m-ZrO$_2$ (wt%)
ZnO-s-30	99.02	0.98	—
ZnO-s-90	98.01	1.11	0.88
ZnO-s-300	97.02	2.28	0.90

Raman and infrared active, E_2 modes are Raman active only and B_1 modes are both Raman and infrared inactive (silent modes) [27]. Polar phonon modes (A_1 and E_1 modes) split into the longitudinal-optical (LO) and transverse-optical (TO) phonons with different frequencies due to the macroscopic electric fields associated with the LO phonons [1, 28]. Non-polar E_2 phonon modes have two frequencies. The low-frequency E_2 mode (E_2^{low}) is associated with vibration of the Zn sublattice, while the high-frequency E_2 mode (E_2^{high}) is related to the vibration of oxygen atoms [29, 30].

We have deconvoluted Raman spectra obtained from our ZnO samples into a series of separated Lorentzian shape peaks by the least-squares optimization method, as shown in figures 4(a) and (b). All peaks observed in samples ZnO-p-0, ZnO-p-300 and ZnO-s-0 can be assigned to the Raman active modes of ZnO crystal. However, in the Raman spectra of the sintered sample ZnO-s-300, additional modes that can be related to the presence of ZrO$_2$ appeared. The frequencies of all Raman peaks assigned to the first- and second-order Raman modes of ZnO are listed in table 3 together with the results for ZnO crystals from the literature [31]. The linewidths of E_2^{high}, E_1(LO) and 2E_1(LO) modes are also presented in table 3.
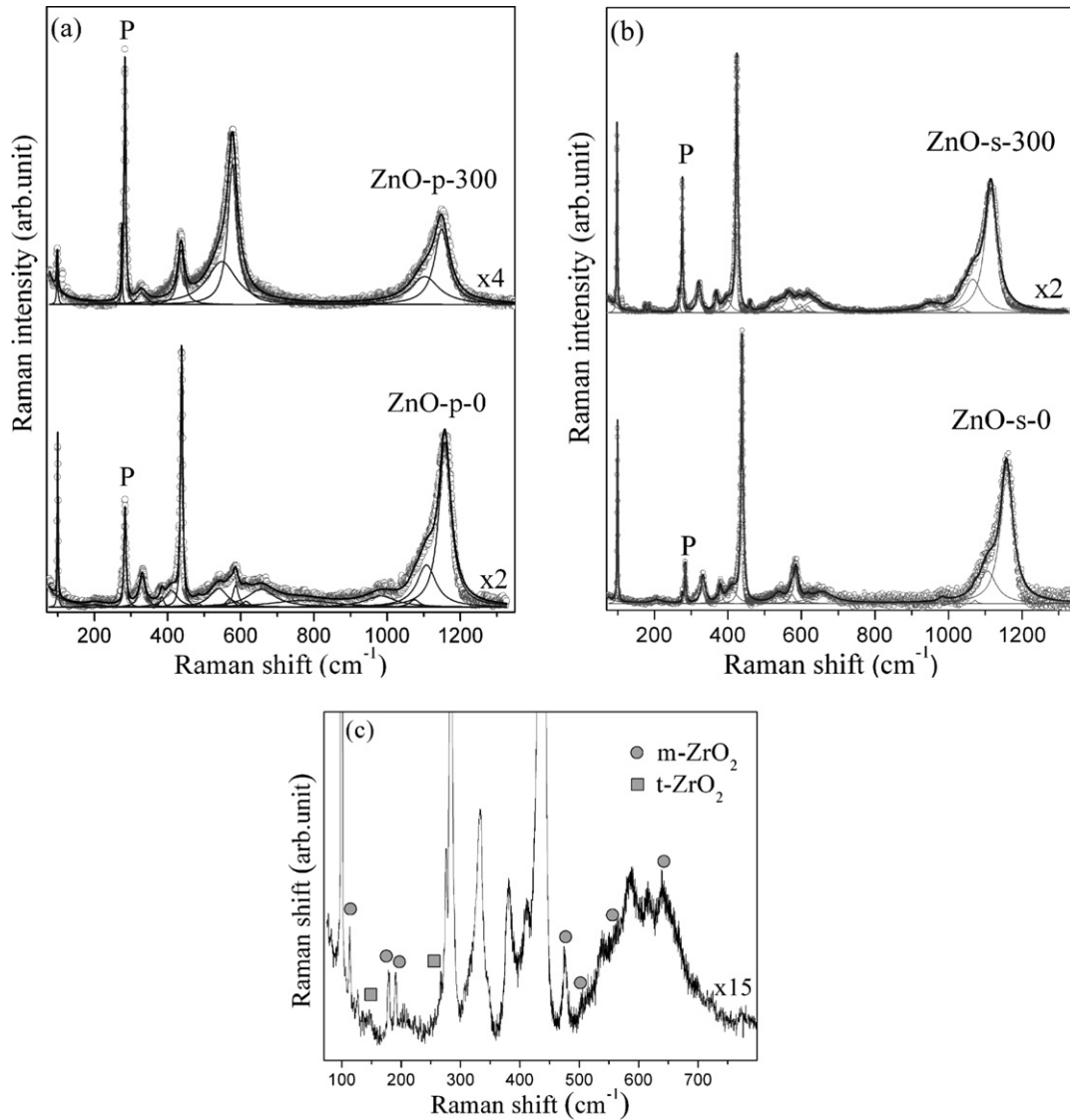
Figure 4. Raman spectra measured by a 442 nm laser line from: (a) ZnO-p-0 and ZnO-p-300 powders and (b) sintered samples ZnO-s-0 and ZnO-s-300 and (c) enlarged part of ZnO-s-300 spectrum with assigned Raman modes originating from m-ZrO$_2$ and t-ZrO$_2$. P denotes plasma lines.

It is evident that Raman modes in the spectrum of unmilled powder ZnO-p-0 have similar positions as in the spectrum of bulk ZnO. However, several changes can be observed in the Raman spectrum of milled powder ZnO-p-300 in comparison with the spectrum of ZnO-p-0. First-order Raman modes, E_2^{low}, E_2^{high}, $E_1(TO)$ and $E_1(LO)$ were redshifted and broadened, while $A_1(TO)$ and $A_1(LO)$ were very hard to resolve after milling. Also, the intense Raman feature at 548 cm^{-1} appears. This feature can be related to the surface optical phonon (SOP) vibrations, as the SOP mode was observed in the Raman spectra of ZnO nanospheres only in the range of 545–565 cm^{-1} [32]. All observed changes could be attributed to the formation of intrinsic defects and a large number of disorderly arranged areas among ultrafine ZnO grains by mechanical activation, combined with the effects of optical phonon confinement in nanosized powders [33–35].

The mode E_2^{high} at $\sim$438 cm^{-1} that is related to the vibration of oxygen atoms in wurtzite ZnO [30] is the most prominent mode in unmilled powder. Drastic decrease of its intensity, a linewidth increase from 6 to 21 cm^{-1} and redshift to the value of about 437 cm^{-1} observed in the Raman spectrum of activated powder all indicate the changes in the defect structure due to mechanical activation. $A_1(LO)$ and especially $E_1(LO)$ modes are strongly affected by defects (such as oxygen vacancy or zinc interstitial or their complexes) or impurity presence [14, 31]. Therefore, the redshift of $E_1(LO)$ from $\sim$586 cm^{-1} (in unmilled powder) to about 578 cm^{-1}, followed by mode intensity and linewidth increase can be related to the enlargement of defect concentration caused by activation. Moreover, a huge increase in the intensity ratio of the $E_1(LO)$ peak to the E_2^{high} peak also points to the defect formation in ZnO powders during mechanical milling [36].

As can be seen from figure 4 and table 3, behavior of the second-order modes in the Raman spectra of activated powder is similar to the behavior of the first-order modes. The intensity of all second-order Raman modes decreases after milling,

Table 3. Raman peak positions observed in various samples and their assignments. Numbers in brackets indicate the FWHM of $E_2^{\rm high}$, E_1(LO) and $2E_1$(LO) modes.

| Process | Raman peak position and FWHM* (cm⁻¹) | | | | |
	ZnO-p-0	ZnO-p-300	ZnO-s-0	ZnO-s-300	Reference[a]
$E_2^{\rm low}$	100	99	99	99	99
2TA; $2E_2^{\rm low}$	203	—	208	—	203
$E_2^{\rm high} - E_2^{\rm low}$	331	329	333	331	333
A_1(TO)	384	—	380	381	378
E_1(TO)	410	—	411	411	410
$E_2^{\rm high}$	438	437	438	438	438
	(6)*	(21)*	(6)*	(7)*	
2LA	483	—	—	—	483
$2B_1^{\rm low}$; 2LA	540	—	538	538	536
SOP		548			
A_1(LO)	570	—	574	579	574
E_1(LO)	586	578	586	586	590
	(18)*	(31)*	(16)*	(31)*	
TA + TO	614	—	618	616	618
TA + LO	656	—	656	656	657
2TO	982	—	984	985	980
TO + LO	—	—	—	—	1044
TO + LO	1075	—	1072	1074	1072
2LO	1108	1103	1106	1105	1105
$2E_1$(LO)	1158	1149	1158	1156	1158
	(40)*	(49)*	(40)*	(41)*	

[a] Reference [31].

Table 4. Intensity ratio of the E_1(LO) peak to the $E_2^{\rm high}$ peak and the ratio of second- to first-order Raman scattering cross section before and after the sintering process.

	ZnO-p-0	ZnO-p-300	ZnO-s-0	ZnO-s-300
$I(E_1({\rm LO})/I(E_2^{\rm high})$	0.25	3.90	0.30	0.29
$I(2{\rm LO})/I({\rm LO})$	16.06	0.84	10.83	10.37

while some of them are redshifted and broadened. However, some of these modes cannot be registered, because it seems they are hidden behind the broad background. It was also found that the electron–LO phonon coupling strength, determined by the ratio of second- to first-order Raman scattering cross sections, $I(2{\rm LO})/I({\rm LO})$, decreases after activation [35, 36].

After sintering, the intensities of the Raman spectra increase, both for ZnO-s-0 and ZnO-s-300 sintered samples. The peak positions revert to values similar to those of the unmilled powder and for ZnO crystals. Also, the linewidths of all modes decrease due to the sintering process. The observed changes in the Raman spectra point to defect annihilation due to the sintering process.

In order to follow the defect structure before and after sintering, the intensity ratio of the E_1(LO) peak to the $E_2^{\rm high}$ peak and the ratio of second-to first-order Raman scattering cross section were determined and are presented in table 4. Decrease in $I(E_1({\rm LO}))/I(E_2^{\rm high})$ and increase of the $I(2{\rm LO})/I({\rm LO})$ ratio after thermal treatment of ZnO-p-300 indicate that the sintering process ensures a reduction in concentration of intrinsic defects primarily related to oxygen vacancies.

The Raman spectrum of sample ZnO-s-300 points to the presence of extrinsic defects related to zirconia introduced during the milling. Namely, additional modes at 113.3, 178.6, 190.7, 266.8, 476.3, 504.6, 560.7 and 638.8 cm⁻¹ in the Raman spectrum of ZnO-s-300 can be assigned to the monoclinic and tetragonal zirconia, as was shown in figure 4(c). The appearance of these modes indicates the presence of zirconia in the form of inclusions. The linewidth of the E_1 (LO) mode in the Raman spectrum of ZnO-s-300 is almost twice as great as in the spectrum of ZnO-s-0, which also points to the increased number of defects in the sample sintered from milled powder.

With the aim of carrying out a detailed investigation of the presence of Zr-related defects in sintered samples, the high resolution Raman spectra of these samples were measured by a triple Raman spectrometer (Jobin-Yvon T64000) and are discussed in next section.

3.3. Micro-Raman spectra of sintered ZnO samples

High resolution Raman spectra measured from the samples obtained by sintering of unmilled powder and those activated for 30, 90 and 300 min are shown in figure 5.

Beside the Raman modes of ZnO, described in the previous section, additional features that can be related to the presence of ZrO_2 were observed in the Raman spectra of all sintered samples prepared from milled powders. The intensity of these additional features apparently increases with increasing activation time of the starting powders.

ZrO_2 has three polymorphs: monoclinic (m-ZrO_2; $P2_1/c$), tetragonal (t-ZrO_2; $P4_2/nmc$) and cubic (c-ZrO_2; $Fm3m$). Group theory analysis indicates that m-ZrO_2 has 18 Raman active modes ($9A_g + 9B_g$), t-ZrO_2 has six Raman active modes ($3E_g + A_{1g} + 2B_{1g}$) and c-ZrO_2 has only one active mode of vibration (F_{2g}). Some Raman features that can be
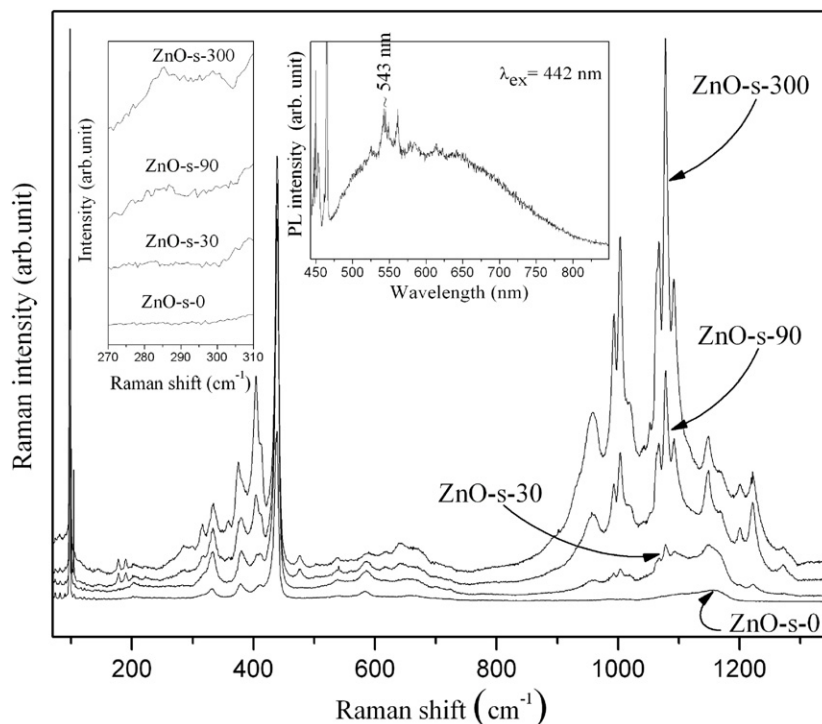
Figure 5. Micro-Raman spectra of sintered samples prepared from the powders obtained after milling in zirconium vials, presented with an increase of milling time. Left inset: evolution of the Raman mode at about 285 cm^{-1} with activation time. Right inset: photoluminescence spectra of the ZnO-s-300 sample excited by the 442 nm line of an HeCd laser.

assigned to the Raman spectra of m-ZrO$_2$ [37] are observed in all sintered samples prepared from milled powders. These modes are at about: 178 (A$_g$), 190 (A$_g$), 476 (A$_g$), 618 (2B$_g$) and 641 cm^{-1} (2A$_g$), while their overtones are at ~959, ~1168 and ~1223 cm^{-1}. The Raman feature at ~147 cm^{-1} that can be assigned to tetragonal ZrO$_2$ [37, 38] and those at about 316 and 358 cm^{-1} that were registered in ZrO$_2$ but without clear assignation [37, 38], are also observed in all samples sintered from milled powders. The intensities of all features related to the presence of ZrO$_2$ in sintered samples increase as milling time of starting powders increases. Moreover, additional modes and overtones that can be assigned to the m-ZrO$_2$ [37] appear in the spectra of ZnO-s-90 and ZnO-s-300 samples at about: 223 (A$_g$), 504 (B$_g$), 560 (A$_g$) and 938 cm^{-1} (overtone). Enhancements of the Raman features assigned to the ZrO$_2$ are a consequence of the increase in concentration of the ZrO$_2$ inclusions, due to ball milling of the starting ZnO powder at various time in the zirconium assembly.

Note also that some kind of resonant enhancement of the higher-order Raman modes of ZnO and ZrO$_2$ in the Raman spectra of sintered samples ZnO-s-t ($t = 30$, 90 and 300 min) is observed. Such enhancement can arise in the vicinity of energy of some electronic transitions. Really, the existence of a photoluminescence (PL) band at an energy of about 2.28 eV (~543 nm) is observed in the PL spectrum of the ZnO-s-300 sample excited by a 442 nm laser line (shown in the right inset of figure 5). This energy just corresponds to the central frequency (~1050 cm^{-1}) of the second-order Raman modes in the spectra of sintered samples excited by a 514.5 nm laser line. It is worth noting that green luminescence at about 530 nm

with similar shape to that registered in the ZnO-s-300 sample was already observed in PL spectra of tetragonal zirconia nanoparticles excited by the 412 nm laser line. This type of luminescence should be related to the involvement of mid-gap trap states, such as surface defects and oxygen vacancies [39].

Finally, it is very important to explain the origin and enhancement of the Raman feature at about 285 cm^{-1}. This feature can be primarily assigned to the $B_1^{high} - B_1^{low}$ silent mode of wurtzite ZnO [31]. It can be related to intrinsic host lattice defects, which either become activated as vibrating complexes or their concentration increases upon dopant or impurity incorporation [40, 41]. The intensity of this Raman mode increases in sintered samples with increasing milling time of starting powder, as can be seen from the left inset of figure 5. Such behavior can be a consequence of incorporation of Zr impurities in the ZnO lattice of sintered ZnO-s-90 and ZnO-s-300 samples. Note that the $B_1^{high} - B_1^{low}$ mode could not be resolved in the Raman spectra of our samples excited by the 442 nm line of an HeCd laser due to the presence of strong plasma lines at 276 and 284 cm^{-1} (see figure 4).

3.4. Resistivity measurements

It was shown that mechanical milling drastically influences the microstructural properties of ZnO powders. The decrease of particle/crystallite size and increase of lattice parameters indicate the gradual variation in concentration of both intrinsic defects and impurities in the form of ZrO$_2$ inclusions or Zr incorporated in the ZnO crystal lattice, introduced in powders during milling. Further, the microstructural and
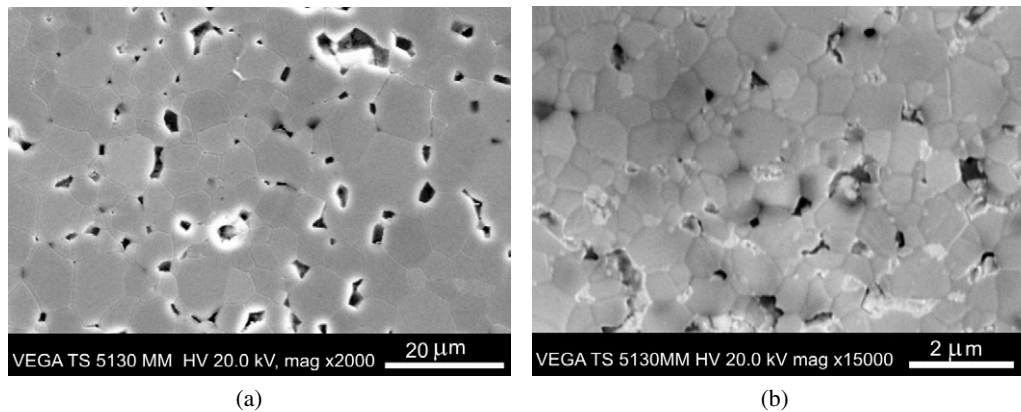
(a)

(b)

Figure 6. SEM micrographs of polished and thermally etched ceramic (a) ZnO-s-0 and (b) ZnO-s-300.
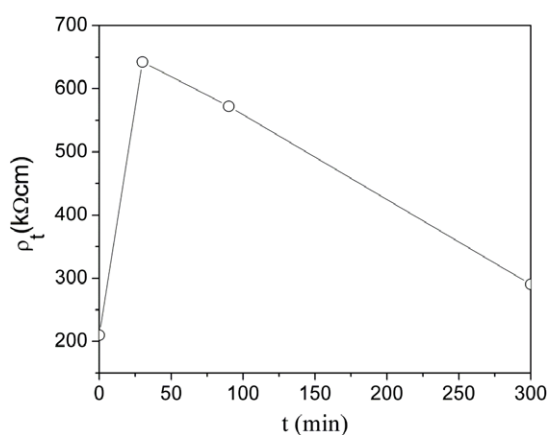

Figure 7. The dependence of electrical resistivity (ρ_{tot}) on milling time.

especially electrical properties of sintered ZnO samples are also influenced by the presence of these defects. As can be seen from figure 6, there is a dense structure with large grains in the range from 3 to 5 μm in the sintered sample ZnO-s-0, while the mechanical milling significantly lowers the grain size to values below 1 μm in ZnO-s-300.

First of all, mechanical milling leads to decrease of grain size and increase of porosity, which have a major effect on electrical properties of polycrystalline materials. Gradual reduction of grain size, i.e. the increase of potential barriers per length unit, consequently results in a higher resistance of sintered samples. Also, the presence of ZrO_2 might have some influence on resistance. The impedance analysis was performed on all sintered samples and the total resistance (R_{tot}) was determined for all samples using fitting results obtained by program ZView. These values were used to calculate the total resistivity, ρ_{tot} (see figure 7).

It was observed that the resistivity rapidly increases with the increase of milling time up to 30 min, as a consequence of the higher number of potential barriers per length unit. Further, the resistivity decreases as the ZrO_2 content increases with milling times longer than 30 min. That could be the result of replacement of Zn^{2+} by Zr^{4+} ions, which was detected by XRD measurements and Rietveld analysis. A similar behavior of the

resistivity was observed in ZnO thin films doped with ZrO_2, when the ZrO_2 content increases from 0 to 5 wt% [19, 20].

4. Conclusions

In summary, ZnO nanoparticles with crystallite sizes of 15 nm were synthesized by mechanical milling for a shorter time (300 min) than has been reported in the literature. Deviation of lattice parameters from single crystal values, obtained after Rietveld powder refinement, reflects the defect creation and increase of strain inside the hexagonal lattice of milled ZnO nanoparticles. Also, the redshift of the major first-order Raman modes ($\sim$2–8 cm^{-1}) and peak broadening are consequences of the intrinsic defect formation by mechanical milling, combined with confinement size effects. The appearance of the intense peak at 548 cm^{-1} that can be related to a surface optical phonon mode confirmed the presence of a large number of disorderly arranged areas among ultrafine ZnO grains in 300 min milled powder.

The Rietveld analysis of the XRD spectra of all sintered samples showed that the strain in sintered ZnO samples drastically decreases in comparison to its value in the starting powders. Further, the intensity of the Raman spectrum increases and the peak positions revert to values similar to those of the unmilled ZnO powder, pointing to defect annihilation after thermal treatment.

XRD spectra of samples prepared by sintering of milled powders show the existence of ZrO_2. Also, the Rietveld analysis reveals that a small number of Zr ions are introduced into the ZnO crystal lattice on the Zn sites or interstitial sites. There is a large influence of those impurities (ZrO_2 or incorporated Zr ions) on the micro-Raman spectra of sintered samples. The additional modes found in the Raman spectrum of the ZnO-s-300 sample suggest the presence of extrinsic defects related to zirconia introduced from the zirconia milling assembly. The enhancement of Raman features assigned to ZrO_2 is a consequence of increased concentration of ZrO_2 inclusions, due to an increase of milling time of the starting powder. Finally, the enhancement of the mode at 285 cm^{-1} as a consequence of dopant or impurity presence, points to the incorporation of Zr ions in the ZnO lattice, which occurs during

the milling of the starting powder. This is in agreement with the results of resistivity measurements, where relatively low resistivity was found in ZnO-s-90 and ZnO-s-300 samples.

This study confirmed the possibility of nanoparticle production by short time milling as well as the importance of the selection of the milling assembly, milling conditions and further thermal treatment in the preparation of powders and ceramics. This way mechanically induced defects (intrinsic and extrinsic) in both powders and sintered samples can be successfully detected by XRD and Raman spectroscopy. Although the increase of resistivity was expected as a consequence of the increasing number of potential barriers per length unit due to the decrease of grain size, the opposite situation occurred. Diffusion of tetravalent Zr into the ZnO lattice, especially on the divalent Zn sites lowered the resistivity and changed the semiconducting properties of ZnO ceramics. This should be seriously considered, especially in the case of milled powders or ceramics produced for electronic use or for further preparation of Zr-doped ZnO films by pulsed-laser deposition or the radio frequency magnetron sputtering method.

Acknowledgments

References

[1] Özgür Ü, Alivov Ya I, Liu C, Teke A, Reshchikov M A, Doğan S, Avrutin V, Cho S-J and Morkoç H 2005 *J. Appl. Phys.* **98** 041301
[2] Ying K-L, Hsieh T-E and Hsieh Y-F 2008 Colloidal dispersion of nano-scale ZnO powders using amphibious and anionic polyelectrolites *Ceram. Int.* at press doi:10.1016/j.ceramint.2008.05.014
[3] Hendrikse K G, Mcgill W J, Reedijk J and Nieuwenhuizen N J 2000 *J. Appl. Polym. Sci.* **78** 2290
[4] Choi M J, McBean K E, Ng P H R, McDonagh A M, Maynard P J, Lennard C and Roux C 2008 *J. Mater. Sci.* **43** 732
[5] Wu Y L, Fu S, Tok A I Y, Zeng X T, Lim C S, Kwek L C and Boey F C Y 2008 *Nanotechnology* **19** 345605
[6] Huang M H, Mao S, Feick H, Yan H Q, Wu Y Y, Kind H, Weber E, Russo R and Yang P D 2001 *Science* **292** 1897
[7] Wang Z L and Song J H 2006 *Science* **312** 242
[8] Yang J L, An S J, Park W I, Yi G C and Choi W 2004 *Adv. Mater.* **16** 1661
[9] Schmidt-Mende L and MacManus-Driscoll J L 2007 *Mater. Today* **10** 40
[10] Karpina V A *et al* 2004 *Cryst. Res. Technol.* **39** 980
[11] Gusev A I and Kurlov A S 2008 *Nanotechnology* **19** 265302
[12] Kakazey M G, Melnikova V A, Sreckovic T, Tomila T V and Ristic M M 1999 *J. Mater. Sci.* **34** 1691
[13] Vojisavljevic K, Zunic M, Brankovic G and Sreckovic T 2006 *Sci. Sinter.* **38** 131
[14] Giri P K, Bhattacharyya S, Singh D K, Kesavamoorthy R, Panigrahi B K and Nair K G M 2007 *J. Appl. Phys.* **102** 093515
[15] Moribe S, Ikoma T, Akiyama K, Zhang Q, Saito F and Tero-Kubota S 2007 *Chem. Phys. Lett.* **436** 373
[16] Suryanarayana C 2001 *Prog. Mater. Sci.* **46** 1
[17] Avvakumov E, Senna M and Kosova N 2001 *Soft Mechanochemical Synthesis* (London: Kluwer–Academic)
[18] Zhang W, Wang H, Liao Y and Yin Y 1993 *Catal. Lett.* **20** 243
[19] Lv M, Xiu X, Pang Z, Dai Y, Ye L, Cheng C and Han S 2008 *Thin Solid Films* **516** 2017
[20] Qadri S B, Kim H, Horwitz J S and Chrisey D B 2000 *J. Appl. Phys.* **88** 6564
[21] Dutta S, Chattopadhyay S, Sutradhar M, Sarkar A, Chakrabarti M, Sanyal D and Jana D 2007 *J. Phys.: Condens. Matter* **19** 236218
[22] Sanyal D, Roy T K, Chakrabarti M, Dechoudhury S, Bhowmick D and Chakrabarti A 2008 *J. Phys.: Condens. Matter* **20** 045217
[23] Dutta S, Chattopadhyay S, Jana D, Banerjee A, Manik S, Pradhan S K, Sutradhar M and Sarkar A 2006 *J. Appl. Phys.* **100** 114328
[24] Srećković T, Bernik S, Čeh M and Vojisavljević K 2008 Microstructural characterization of mechanically activated ZnO powders *J. Microsc.* at press
[25] Coelho A 2007 Topas-Academic V4.1, http://members.optusnet.com.au/~alancoelho/
[26] Wang F, Lv M, Pang Z, Yang T, Dai Y and Han S 2008 Theoretical study of structural, optical and electrical properties of zirconium-doped zinc oxide *Appl. Surf. Sci.* **234** 6983
[27] Zhou H, Chen L, Malik V, Knies C, Hofmann D M, Bhatti K P, Chaudhary S, Klar P J, Heimbrodt W, Klingshirn C and Kalt H 2007 *Phys. Status Solidi* a **204** 112
[28] Wang J Z, Peres M, Soares J, Gorochov O, Barradas N P, Alves E, Lewis J E, Fortunato E, Neves A and Monteiro T 2005 *J. Phys.: Condens. Matter* **17** 1719
[29] Lin K F, Cheng H M, Hsu H C and Hsieh W F 2006 *Appl. Phys. Lett.* **88** 263117
[30] Alim K A, Fonoberov V A, Shamsa M and Balandin A A 2005 *J. Appl. Phys.* **97** 124313
[31] Cuscó R, Alarcón-Lladó E, Ibáñez J and Artús L 2007 *Phys. Rev.* B **75** 165202
[32] Zeng H, Cai W, Cao B, Hu J, Li Y and Liu P 2006 *Appl. Phys. Lett.* **88** 181905
[33] Alim K A, Fonoberov F A and Balandin A A 2005 *Appl. Phys. Lett.* **86** 053103
[34] Du Y, Zhang M-S, Hong J, Shen Y, Chen Q and Yin Z 2003 *Appl. Phys.* A **76** 171
[35] Šćepanović M, Srećković T, Vojisavljević K and Ristić M M 2006 *Sci. Sinter.* **38** 169
[36] Wang R P, Xu G and Jin P 2004 *Phys. Rev.* B **69** 113303
[37] Siu G G, Stokes M J and Liu Y 1999 *Phys. Rev.* B **59** 3173
[38] Anastassakis E, Papanicolaou B and Asher I M 1975 *J. Phys. Chem. Solids* **36** 667
[39] Liang J, Deng Z, Jiang X, Li F and Li Y 2002 *Inorg. Chem.* **41** 3602
[40] Bundesmann C, Ashkenov N, Schubert M, Spemann D, Butz T, Kaidashev E M, Lorenz M and Grundmann M 2003 *Appl. Phys. Lett.* **83** 1974
[41] Hasuike N, Fukumura H, Harime H, Kisoda K, Matsui H, Saeki H and Tabata H 2004 *J. Phys.: Condens. Matter* **16** S5807